Implications of Remote Water Molecules on the Electron Transfer Coupled Processes at a Nonporphyrinic Mn(III)-hydroxido Complex

Sanae El Ghachtouli,[a,b] Benedikt Lassalle-Kaiser,[b,c] Pierre Dorlet,[d] Regis Guillot,[b] Elodie Anxolabéhère-Mallart,[a*] Cyrille Costentin,[a*] and Ally Aukauloo [b,e *]

Received (in XXX, XXX) Xth XXXXXXXXX 20XX, Accepted Xth XXXXXXXXX 20XX
DOI: 10.1039/b000000x

Supplementary Information

Table of content

I. Experimental Section

II. Crytallographic Data

III. Controlled potential electrolysis of 1$^+$ in reduction.

IV. $^{18}O/^{16}O$ exchange on 1$^+$

V. Controlled potential electrolysis of 1$^+$ in oxidation.

I. Experimental Section

Reagents and solvents were purchased commercially and used as received except for electrochemical experiments. $H_2^{18}O$ was purchased from Eurisotop, (isotopic enrichment 95,4%)

Caution: Perchlorate salts of metal complexes with organic ligands are potentially explosive. Only small quantities of these compounds should be prepared and they should be handled behind suitable protective shields.

Scheme S1: ligand *tBu*L$^-$

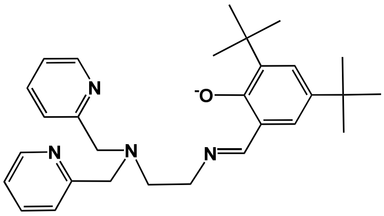

Complex synthesis:

[*tBu*LMn(III)OH](ClO_4)] (**1**(ClO_4)): 212 mg (0.88 mmol) of 3,5-Di-tert-butyl-2-hydroxybenzaldehyde[1] and 207 mg (0.88 mmol, 1 eq.) of N,N-dipyridyléthanediamine[2] were stirred under an argon atmosphere for 2 h in 10 mL of ethanol. One equivalent of triethylamine (122 µL, 0.88 mmol) and $Mn(ClO_4)_2.6(H_2O)$ (318 mg, 0.88 mmol.), dissolved in 5 mL of acetonitrile were then added to the mixture. The brown-red solution was stirred for an additional 2 h. The resulting solution was poured onto water (70 mL) to provide a green-brown precipitate that was collected by filtration, and washed with a minimum of ethanol and diethyl ether. After drying under vacuum a brown solid is obtained with 70 % yield. Single crystals suitable for X-ray analysis were produced by slow evaporation of an ethanolic solution of **1**(ClO_4). Elemental analysis for [*tBu*LMn(III)OH](ClO_4)]: $MnC_{29}H_{38}N_4ClO_6$ calcd (%): C 55.37, H 6.09, N 8.91; found (%): C 55.14, H 6.07, N 8.81. ESI MS : m/z = 529.2 [(*tBu*L)Mn(III)OH]$^+$. IR: ν (OH) = 3650 cm^{-1}, ν (Mn-O) = 607 cm^{-1}

Elemental analyses were carried out at the Services de Microanalyse, ICSN-CNRS, Gif-sur-Yvette, France.

Electrospray Ionization Mass Spectrometry. Mass spectra were recorded with a Finnigan MAT95S in a BE configuration at low resolution on micromolar acetonitrile solution.

NMR spectroscopy: ^{1}H-NMR spectra were recorded on a Bruker DPX 300 MHz with a ONP probe at room temperature in d_1-$CDCl_3$ ($\delta = 7.24$ ppm).

IR spectroscopy: IR spectra were recorded by means of a Fourier Transform Perkin–Elmer 100, using KBr solid solution (1% compound in mass), over the range 4000-400 cm^{-1}, at room temperature.

EPR spectroscopy: 9.4 GHz EPR (X-band) spectra were recorded on a Bruker ELEXSYS 500 spectrometer equipped with an Oxford Instrument continuous flow liquid helium cryostat and a temperature control system. A dual mode cavity (Bruker ER 4116DM) was used for perpendicular and parallel mode detection, respectively. Solutions spectra were recorded in MeCN containing 0.2 M Bu_4NPF_6.

Cyclic voltammetry and bulk electrolysis. All electrochemical experiments were run under Argon atmosphere. Cyclic voltammetry and coulometry measurements were recorded either on an EGG PAR potentiostat (M273 model) or a Metrohm potentiostat (AUTOLAB model). For cyclic voltammetry, the counter electrode used was a Pt wire and the working electrode a glassy carbon disk carefully polished before each voltammogram with a 1 μm diamond paste, sonicated in ethanol bath and then washed with ethanol. The reference electrode used was an Ag/$AgClO_4$ electrode with acetonitrile as solvent (0.3 V *vs.* SCE electrode), isolated from the rest of the solution by a fritted bridge. For bulk electrolysis, the counter electrode used was a piece of Pt, separated from the rest of the solution with a fritted bridge. The working electrode was a cylinder of glassy carbon. Supporting electrolyte NBu_4PF_6 (Aldrich, puriss) was 0.1 M (20°C) or a 0.2 M (low temperature) in acetonitrile (Aldrich, puriss). Low temperature regulation was ensured by a Julabo circulation cryostat.

In the case of experiments for which water has been added to the initially dry acetonitrile solution, modification of the junction potential upon water addition may induce a shift in teh potential values. Controlled experiments carried out with ferrocene showed a shift of 40 mV towards negative potentials for the $[H_2O]$ = 11M and of 60 mV for $[H_2O]$ = 22M (see Table S1)

Table S1: Shift of the $E^{1/2}$ value for a 1 mM Ferrocene solution in 5 mL dry CH_3CN+ $TBAPF_6$ 0.1 M upon addition of increasing amount of distilled water.

$[H_2O]$ (M)	$E^{1/2}$ (V vs SCE)	$\Delta(E^{1/2} - E^{1/2}_{[H2O]})$ (mV)
0	0.386	0
5.5	0.357	29
11	0.346	40
16.5	0.335	51
22	0.326	60

Single-crystal X-ray structure analyses: Details of the crytal data, data collection and refinement are given in Table S2. The diffraction intensities were collected with graphite-monochromatized Mo Kα radiation. Data collection and cell refinement were carried out using a Brucker Kappa X8 APEX II diffractometer. The temperature of the crystal was maintained at the selected value (100K) by means of a 700 series Cryostream cooling device to within an accuracy of ±1 K. Intensity data were corrected for Lorenz-polarization and absorption factors. The structures were solved by direct methods using SHELXS-97,[3] and refined against F^2 by full-matrix least-squares methods using SHELXL-97[3] with anisotropic displacement parameters for all non-hydrogen atoms. All calculations were performed by using the Crystal Structure crystallographic software package WINGX.[4]

Treatment on H: H atoms of the ligand were added from the difference Fourier map, and refined by the riding model. The H atoms of the water molecules were subsequently included in the refinement in geometrically idealized positions, with C—H = 0.96(3) Å H-H = 1.52(3) Å, and refined using the riding model with isotropic displacement parameters of Uiso(H) = 1.5Ueq (parent atom).

CCDC 781528 contains the supplementary crystallographic data for this paper. These data can be obtained free of charge from the Cambridge Crystallographic Data Centre via www.ccdc.cam.ac.uk/data_ request/cif.

II. Crytallographic Data

Figure S1: representation of the two structural motifs found in the unit cell (Mn1 in site 1; Mn02 in site 2) showing the surrounding water molecules.

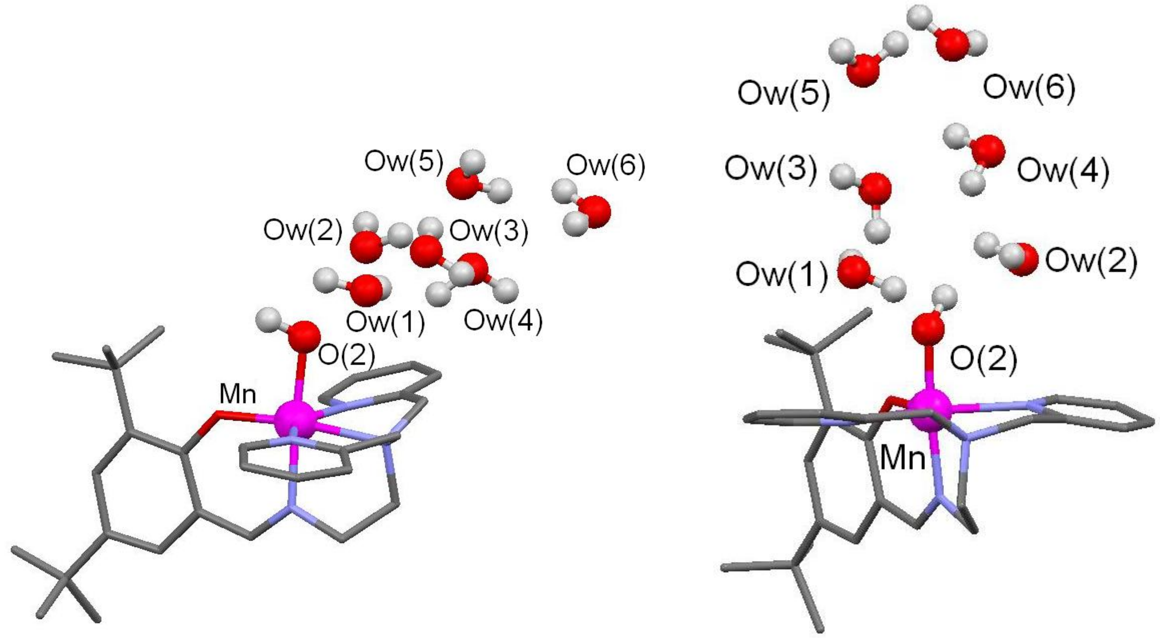

Site 1 **Site 2**

Two additional views of the manganese complex showing for each site the water molecules (red and orange colours) surrounding the Mn(III)-OH fragment, one perchlorate anion attributed to each manganese complex. For geometric consideration, a centre of inversion is indicated in blue.

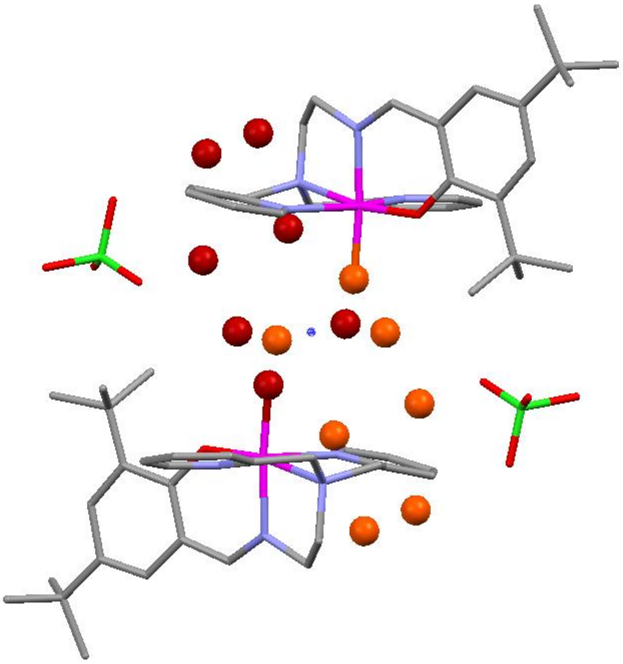

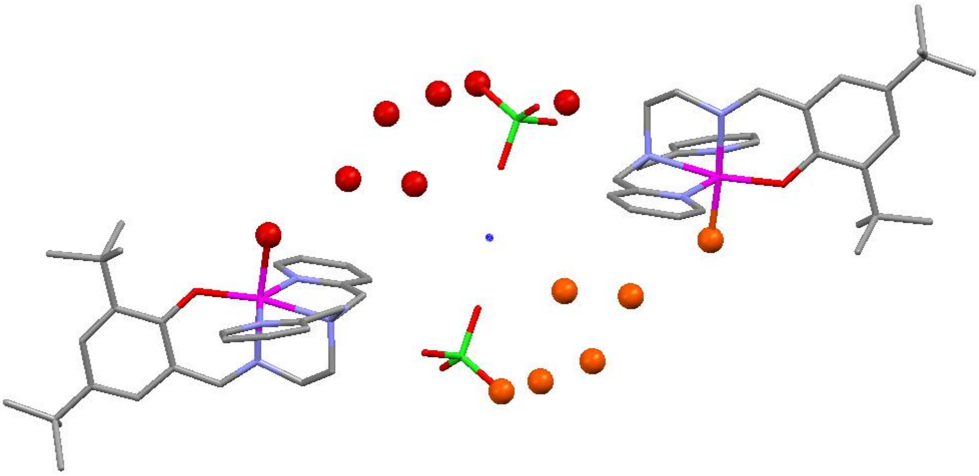

Table S2. Crytallographic Data for **1**(ClO_4).

Empirica formula	$C_{58} H_{88} Cl_2 Mn_2 N_8 O_{18}$
Formula weight	1366.14
Temperature (K)	100(1)
Wavelength (Å)	0.71069
Crystal system	triclinic
Space group	P -1
Unit cell dimensions	
a (Å)	13.020(5)
b (Å)	15.733(5)
c (Å)	17.847(5)
α (°)	103.308(5)
β (°)	102.881(5)
γ (°)	100.429(5)
V (Å^3)	3362.5(19)
Z	2
$D_{calc.}$ ($Mg.m^{-3}$)	1.349
Absorption coefficient (mm^{-1})	0.527
F (0 0 0)	1440
Reflection collected	14942
Independent reflections (Rint)	6536 (0.1032)
Observed reflections ($I > 2\sigma(I)$)	3295
Final *R* indices [$I > 2\sigma I$]	R1=0.0855, wR2=0.2110
S	1.049
$(\Delta \rho)_{max, min}$ [e Å^{-3}]	0.909 ; -0.521

Table S3. Selected bond lengths [Å] and angles [°] for **1**$^+$.

Lengths [Å]			
Site 1		**Site 2**	
Mn – O(1)	1.88(3)	Mn – O(1)	1.89(3)
Mn – N(1)	1.98(3)	Mn – N(1)	1.97(4)
Mn – N(2)	2.16(4)	Mn – N(2)	2.16(4)
Mn – N(3)	2.25(4)	Mn – N(3)	2.21(4)
Mn – N(4)	2.21(4)	Mn – N(4)	2.23(4)
Mn – O(2)	1.97(3)	Mn – O(2)	1.86(3)
O(2) –Ow(1)	2.85	O(2) –Ow(1)	2.76
Ow(1) – Ow(2)	2.50	O(2) – Ow(2)	2.60
Ow(1) – Ow(3)	2.47	Ow(1) – Ow(3)	3.73
Ow(2) – Ow(3)	3.56	Ow(2) – Ow(4)	3.15
Ow(2) – Ow(4)	3.15	Ow(3) – Ow(4)	2.71
Ow(2) – Ow(5)	2.70	Ow(3) – Ow(5)	2.76
Ow(4) – Ow(5)	3.89	Ow(4) – Ow(6)	2.50
Ow(5) – Ow(6)	3.73	Ow(5) – Ow(6)	2.47
Angles [°]*			
O(1) – Mn – O(2)	94.1(14)	N(1) – Mn – N(4)	85.4(14)
O(1) – Mn – N(1)	90.2(14)	N(2) – Mn – N(3)	74.5(15)
O(1) – Mn – N(2)	169.3(14)	N(2) – Mn – N(4)	77.6(15)
O(1) – Mn – N(3)	99.8(15)	N(2) – Mn – O(2)	94.6(15)
O(1) – Mn – N(4)	108.5(16)	N(3) – Mn – N(4)	151.7(17)
N(1) – Mn – N(2)	81.3(15)	N(3) – Mn – O(2)	86.8(14)
N(1) – Mn – O(2)	175.0(16)	N(4) – Mn – O(2)	90.8(14)
N(1) – Mn – N(3)	94.8(14)		

* mean values between site 1 and 2 of the unit.

III. Controlled potential electrolysis of 1^+ in reduction.

Figure S2: EPR spectrum of a 2 mM solution of 1(ClO_4) in dry CH_3CN + 0.1 M NBu_4PF_6 before (1) and after (1red) exhaustive reduction −0.64 V *vs* SCE; *T*=293 K, working electrode: glassy carbon crucible; auxiliary electrode: Pt grid separated from the rest of the solution with a fritted glass. EPR recording conditions: microwave frequency 9.634 GHz, microwave power 1 mW (for 1 and 1red 15K) and 0.25 mW (for 1red 3.7K), modulation amplitude 0.8 mT, temperature as indicated.

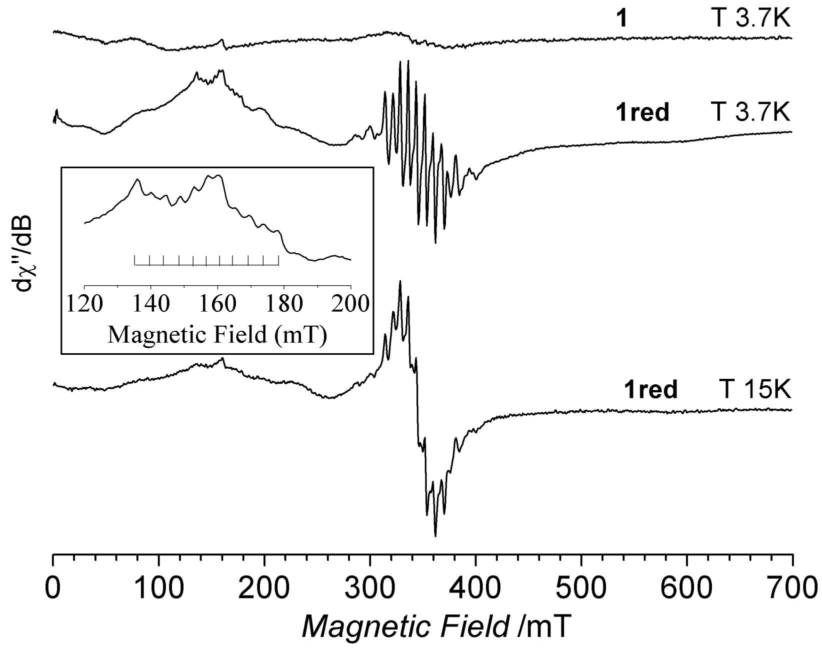

The resonances observed in the EPR spectra after reduction are compatible with a weakly coupled Mn(II) dimer species. More specifically, the drastic temperature dependence of the spectrum indicates a coupled spin system and the resolved 11-line hyperfine structure observed around 160 mT with an average splitting of 4.2 mT supports a homovalent Mn(II) dimer. Nevertheless, a mixture of species in solution cannot be excluded completely. In particular, part of the signal at g=2 (350 mT) could be due to the presence of some Mn(II)Mn(III) mixed-valent complex coming from incomplete reduction.

IV. $^{18}O/^{16}O$ exchange on 1^{+}

Figure S3: ESI-MS on **1**(ClO_4) in CH_3CN (1mM) (a); after addition of 520 µL of $^{18}OH_2$ (b).

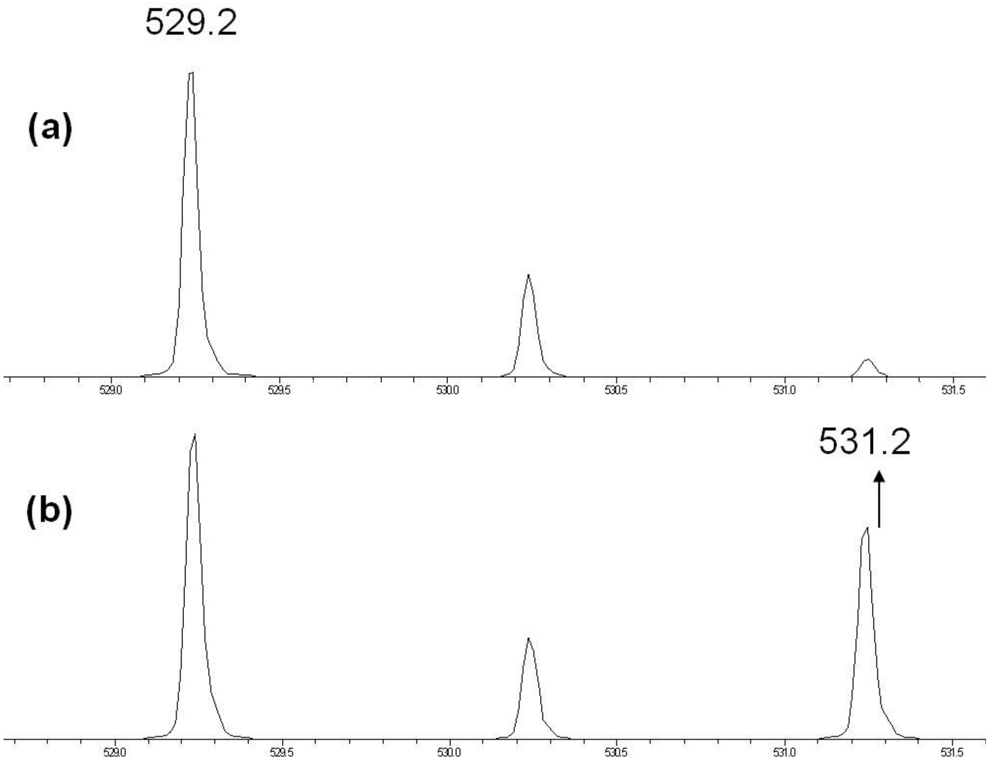

Before addition of $^{18}OH_2$: m/z = 529.2 $[Mn(tBuL)(^{16}OH)]^{+}$

After addition of $^{18}OH_2$: m/z = 531.2 $[Mn(tBuL)(^{18}OH)]^{+}$

V. Controlled potential electrolysis of 1^+ in oxidation.

Figure S4. EPR spectrum of a 2 mM solution of **1**(ClO_4) in CH_3CN + 0.1 M NBu_4PF_6 after exhaustive electrolysis at + 1 V *vs* SCE in the presence of an excess of 2,6-dimethylpyridine; *T*=293 K, working electrode: glassy carbon crucible; auxiliary electrode: Pt grid separated from the rest of the solution with a fritted glass. EPR recording conditions: microwave frequency 9.498 GHz, microwave power 16 μW, modulation amplitude 2 mT, *T*=10 K.

The EPR spectrum confirms the presence of mixed valent oxo-bridged Mn(III)Mn(IV) complex. Similar electrochemical formation of dinuclear oxo-bridged Mn(III)Mn(IV) complexes has been reported previously.[5-8]

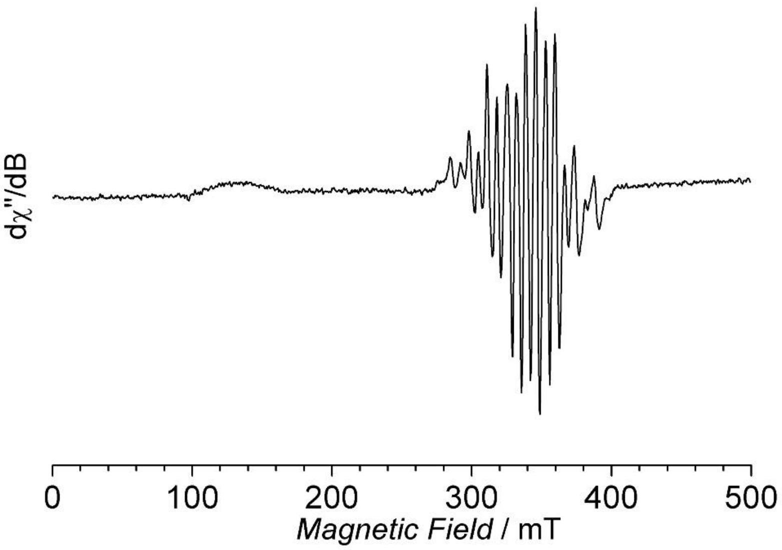

Figure S5: Cyclic votammetry of 2 mM solution of **1**(ClO_4) in CH_3CN + 0.1 M NBu_4PF_6 + 13 M H_2O before (solid line) and after (dashed line) exhaustive oxidative electrolysis at 1 V vs SCE.

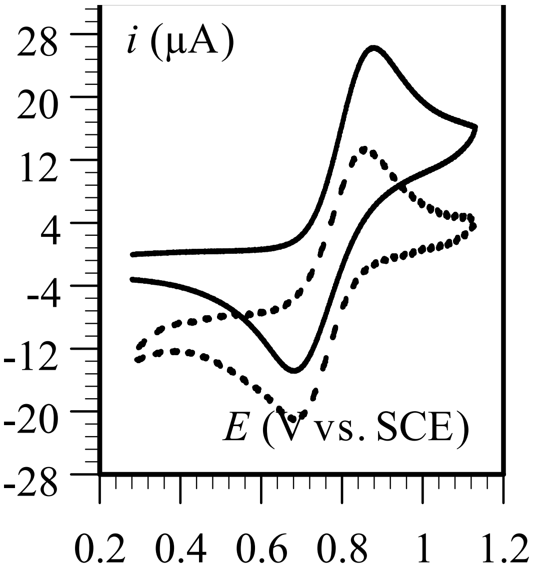

Figure S6: EPR spectra of 2 mM solution of **1**(ClO_4) in CH_3CN + 13 M H_2O + 0.1 M NBu_4PF_6 before (**1**$^+$) and after (**1ox**) exhaustive oxidative electrolysis at 1 V vs SCE. Experimental conditions: 2mM solution in acetonitrile (0.1 M Bu_4NPF_6). Recording conditions: microwave frequency 9.63 GHz, microwave power 1 mW, modulation amplitude 1mT, time constant 160ms, T 5K.

The spectrum of **1**$^+$ is essentially silent in perpendicular mode as expected for a Mn(III) species. For **1ox**, the resonance around 150 mT can be attributed to an electronic spin 3/2 and supports the formation of a mononuclear Mn(IV) species upon electrolysis. The spectrum is similar to what is routinely observed for such species.

We note for the spectrum of **1ox** the presence of the characteristic six-line signal at g = 2 (350 mT) corresponding to Mn(II)(H_2O)$_6$ impurity. The Mn(II) amount is estimated by titration to account for less than 10 % of the total amount of Mn ion.

Signal at g = 2 in the spectrum of **1** is attributed to a radical impurity.

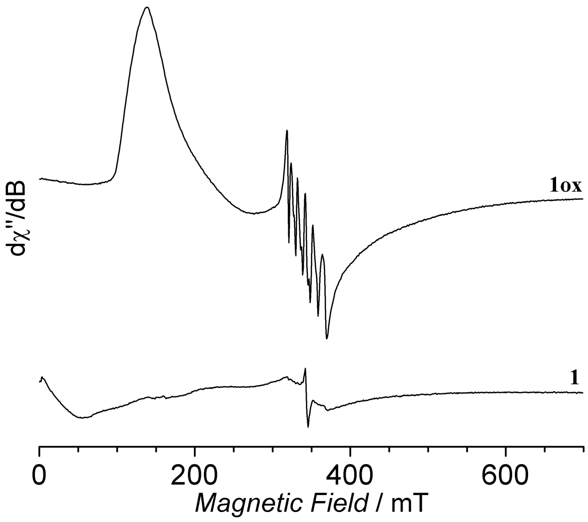

VI. Isotope effects (D_2O or $^{18}H_2O$) on the cyclic voltametry of 1^+ in oxidation:

Figure S7: Cyclic votammetry of 2 mM solution of **1**(ClO_4) in CH_3CN + 0.1 M NBu_4PF_6, *T*=293 K. Solid line: in presence of 10 M of H_2O; dashed line: in presence of 10 M of D_2O.

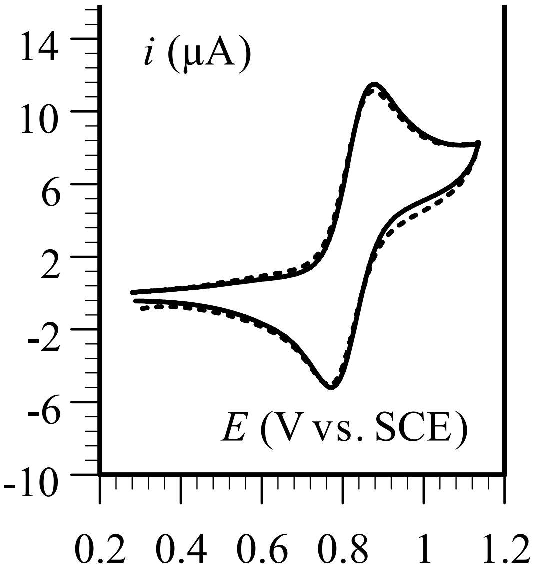

Figure S8: Cyclic votammetry of 2 mM solution of **1**(ClO_4) in CH_3CN + 0.1 M NBu_4PF_6, *T*=293 K. Dashed line: in presence of 10 M of H_2O; solid line: in presence of 10 M of $^{18}OH_2$.

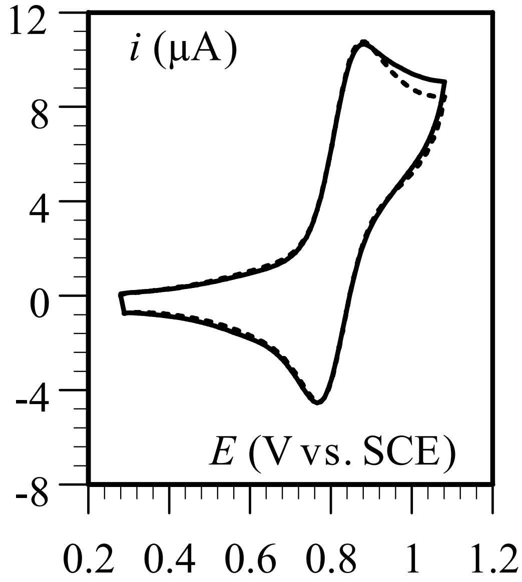

VII. Detailed analysis of the variation of the shape of the Mn(III/Mn(II) wave upon of addition of H_2O. Description of the zone diagram for an EC_{-2} mechanism.

Zone diagram for the EC_{-2} mechanism :

In order to prove that the shape of the voltammograms obtained experimentally upon addition of water (figure 2) may be interpreted in the framework of a mechanism corresponding to equations (1-1) and (1-2) and corresponds to the situation where the backward chemical reaction interferes kinetically with diffusion, we will use the zone diagram corresponding to this mechanism. To the best of our knowledge, the zone diagram corresponding to this mechanism has not been yet reported although zone diagrams for closely related mechanisms have been described in the literature.[9]

We will first present the construction of the zone diagram (figure S9) in order to give the parameters upon which the voltammogram shapes depend. Then we will use the zone diagram to interpret the experimental results and finally do simulations of the voltammograms with pertinent set of parameters.

a. Construction of the zone diagram:

We consider the following EC_{-2} mechanism (-2 subscript indicates that the backward reaction is a second order reaction whereas the forward reaction is pseudo-first order) in which water is in large excess:

$$[\mathrm{Mn^{III}OH}]^{+} + e^{-} \rightleftharpoons [\mathrm{Mn^{II}OH}]$$

$$[\mathrm{Mn^{II}OH}] \underset{k_-}{\overset{k_+[\mathrm{H_2O}]}{\rightleftharpoons}} [\mathrm{Mn^{II}OH_2}]^{+} + \mathrm{OH}^{-}$$

As shown below, the characteristics of the voltamogramms corresponding to this mechanism depends upon two dimensionless parameters: $K = \dfrac{k_+[\mathrm{H_2O}]}{k_- C^0}$ and $\lambda_+ = \dfrac{RT}{Fv} k_+[\mathrm{H_2O}]$. The analysis is based on the same grounds as already used for several mechanisms in the literature.[9]

The reaction scheme gives rise to the following set of partial derivative equations:

(for the sake of simplicity we note $[\mathrm{Mn^{III}OH}]^{+}$ = A , $[\mathrm{Mn^{II}OH}]$ = B, $[\mathrm{Mn^{II}OH_2}]^{+}$= C, OH^{-} = D)

$$\frac{\partial[\mathrm{A}]}{\partial t} = D\frac{\partial^2[\mathrm{A}]}{\partial x^2}$$

$$\frac{\partial[\mathrm{B}]}{\partial t} = D\frac{\partial^2[\mathrm{B}]}{\partial x^2} - k_+[\mathrm{H_2O}][\mathrm{B}] + k_-[\mathrm{C}][\mathrm{D}]$$

$$\frac{\partial[\mathrm{C}]}{\partial t} = D\frac{\partial^2[\mathrm{C}]}{\partial x^2} + k_+[\mathrm{H_2O}][\mathrm{B}] - k_-[\mathrm{C}][\mathrm{D}]$$

$$\frac{\partial[\mathrm{D}]}{\partial t}=D\frac{\partial^2[\mathrm{D}]}{\partial x^2}+k_+\left[\mathrm{H_2O}\right][\mathrm{B}]-k_-[\mathrm{C}][\mathrm{D}]$$

The initial and boundary conditions for the systems are:

$t=0, x\geq 0$ and $t\geq 0, x=\infty$:

$$[\mathrm{A}]=C^0,\ [\mathrm{B}]=0\ ,\ [\mathrm{C}]=[\mathrm{D}]=0$$

$t\geq 0, x=0$:

$$\frac{\partial[\mathrm{C}]}{\partial x}=\frac{\partial[\mathrm{D}]}{\partial x}=0,\ \frac{I}{F}=D\left(\frac{\partial[\mathrm{A}]}{\partial x}\right)_{x=0}=-D\left(\frac{\partial[\mathrm{B}]}{\partial x}\right)_{x=0}$$

$$E=E^0+\frac{RT}{F}\ln\left(\frac{[\mathrm{A}]_0}{[\mathrm{B}]_0}\right)$$ assuming fast electron transfer kinetics

A dimensionless formulation of the above equations is obtained by introduction of a series of dimensionless variables:

$$\tau=\frac{Fv}{RT}t,\ y=x\sqrt{\frac{Fv}{RTD}},\ \xi=\frac{F}{RT}\left(E-E^0\right),\ a=\frac{[\mathrm{A}]}{C^0},\ b=\frac{[\mathrm{B}]}{C^0},\ c=\frac{[\mathrm{C}]}{C^0},\ d=\frac{[\mathrm{D}]}{C^0}$$

$$\lambda_+=k_+\left[\mathrm{H_2O}\right]\frac{RT}{Fv},\ \lambda_-=k_-C^0\frac{RT}{Fv},\ K=\frac{\lambda_+}{\lambda_-},\ \psi=\frac{I}{FC^0\sqrt{D}\sqrt{\frac{Fv}{RT}}}$$

We thus obtain:

$$\frac{\partial a}{\partial \tau}=\frac{\partial^2 a}{\partial y^2}$$

$$\frac{\partial b}{\partial \tau}=\frac{\partial^2 b}{\partial y^2}-\lambda_+b+\lambda_-cd$$

$$\frac{\partial c}{\partial \tau}=\frac{\partial^2 c}{\partial y^2}+\lambda_+b-\lambda_-cd$$

$$\frac{\partial d}{\partial \tau}=\frac{\partial^2 d}{\partial y^2}+\lambda_+b-\lambda_-cd$$

The initial and boundary conditions for the systems are:

$\tau=0, y\geq 0$ and $\tau\geq 0, y=\infty$:

$$a=1,\ b=c=d=0$$

$t\geq 0, x=0$:

$$\frac{\partial c}{\partial y}=\frac{\partial d}{\partial y}=0\,,\ \psi=\left(\frac{\partial a}{\partial y}\right)_0=-\left(\frac{\partial b}{\partial y}\right)_0$$

$$\xi=\ln\left(\frac{a_0}{b_0}\right)$$

Then:

$$\frac{\partial(b+c)}{\partial\tau}=\frac{\partial^2(b+c)}{\partial y^2}$$

$$\frac{\partial a}{\partial\tau}=\frac{\partial^2 a}{\partial y^2}$$

Integration leads to:

$$a_0=1-\mathcal{I}\psi \text{ with } \mathcal{I}\psi=\frac{1}{\sqrt{\pi}}\int_0^{\tau}\frac{\psi}{\sqrt{\tau-\eta}}d\eta$$

$$b_0+c_0=\mathcal{I}\psi$$

The equations also show that:

$$\forall\tau \text{ and } \forall y \quad c=d$$

and

$$\frac{\partial a}{\partial\tau}=\frac{\partial^2 a}{\partial y^2}$$

$$\frac{\partial b}{\partial\tau}=\frac{\partial^2 b}{\partial y^2}-\lambda_+\left(b-\frac{c^2}{K}\right)$$

$$\frac{\partial c}{\partial\tau}=\frac{\partial^2 c}{\partial y^2}+\lambda_+\left(b-\frac{c^2}{K}\right)$$

Those equations indicate that, as already mentioned, the systems depends upon two parameters: $\lambda_+=k_+\left[\mathrm{H_2O}\right]\frac{RT}{Fv}$ and $K=\frac{k_+\left[\mathrm{H_2O}\right]}{k\_C^0}$.

The shapes of the voltamogramms obtained depends on the values of those parameters representing the various regimes of kinetics competition between diffusion and follow-up reaction.

Two main situations may be reached depending on whether the chemical equilibrium is fast or not.

(i) fast equilibrium: (λ large) the corresponding zones in the $\log K$ - $\log\lambda_+$ so-called zone diagram (figure S9) are referred to as the D zones indicating pure diffusion control.

If chemical equilibrium is fully achieved, then:

$$K = \frac{c_0^2}{b_0}$$

This leads to:

$$b_0 = \frac{K}{4}\left(\sqrt{1+4\frac{\mathcal{I}\psi}{K}}-1\right)^2$$

and thus the equation of the voltammogram, that only depends on the K parameter, ensues :

$$1-\mathcal{I}\psi = \frac{K}{4}\left(\sqrt{1+4\frac{\mathcal{I}\psi}{K}}-1\right)^2 \exp(\xi)$$

- If K is small, a reversible unperturbed Nernstian wave is obtained leading to the **DO zone** (ordinary diffusion) where the chemical equilibrium has no significant influence:

  $$1-\mathcal{I}\psi = \mathcal{I}\psi\exp(\xi)$$

- If K is large, a reversible wave is obtained whose equation is:

  $$1-\mathcal{I}\psi = \mathcal{I}\psi^2 \exp(\xi') \text{ with } \xi' = \xi - \ln K$$

  The characteristics of this reversible wave are: $\xi'_p = 1.39$, $\psi_p = 0.406$ and $\xi'_p - \xi'_{p/2} = 2.75$ indicating that the wave is much thicker than the Nernstian wave obtained in the DO zone.

  This situation corresponds to the **DE zone** (extraordinary diffusion) which characterizes the reversible reduction of A into an equilibrium mixture of B and C+D with total mobility of the equilibrium.

(ii) irreversible chemical reaction: the corresponding zones in the $\log K$ - $\log \lambda_+$ diagram are referred to as the K zones indicating a kinetic control by the chemical reaction.

We thus consider that pure kinetics condition is fulfilled for B (mutual compensation between diffusion and chemical reaction), *i.e.*:

$$\frac{\partial b}{\partial \tau} = \frac{\partial^2 b}{\partial y^2} - \lambda_+\left(b - \frac{c^2}{K}\right) = 0$$

If the chemical reaction is irreversible (then we can consider that $b >> \frac{c^2}{K}$). The system becomes independent on K and:

$$\frac{\partial^2 b}{\partial y^2} = \lambda_+ b \text{ leading to: } b_0 = \frac{\psi}{\sqrt{\lambda_+}}$$

A completely irreversible voltammogram is thus obtained corresponding to the **KP zone**:

$$1-\mathcal{I}\psi=\frac{\psi\exp(\xi)}{\sqrt{\lambda_+}}$$

(iii) Transition between zones:

Starting from the KP zone and decreasing the value of λ_+ allows to reach the DO zone by crossing an intermediate zone called **KO**.

More interesting for our system are the boundaries between the DE zone and the KP zone (the separation zone is called KE) obtained for large values of K and large values of λ_+ and corresponding to the interference of the backward chemical reaction. Indeed, increasing the concentration of water induces an increase of both K and λ_+ indicating that this situation is the one observed experimentally.

In order to investigate this situation where the total mobility of the chemical equilibrium is no more fulfilled, we consider the following situation as already depicted for reversible dimerization in the literature:[10] λ_+ is large enough so that the chemical reaction is in rapid equilibrium outside a thin reaction layer adjacent to the electrode. Inside this layer ($y\le\mu$) pure kinetic conditions apply to B whereas B, C and D are under diffusion control with $Kb=c\times d=c^2$ outside. We thus have:

For $y<\mu$:

$$\frac{\partial^2 b}{\partial y^2}-\lambda_+\left(b-\frac{c^2}{K}\right)=0$$

Since $b+c\simeq b_0+c_0=\mathcal{I}\psi$:

$$\frac{\partial^2 b}{\partial y^2}=\lambda_+\left(b-\frac{c^2}{K}\right)=\lambda_+\left(b-\frac{(\mathcal{I}\psi-b)^2}{K}\right)\simeq\lambda_+\left(b-\frac{\mathcal{I}\psi^2}{K}\right)$$

because in this region b is small.

Introducing $b'=Kb$ and $y'=Ky$ gives:

$$\frac{\partial^2 b'}{\partial y'^2}=\frac{\lambda_+}{K^2}\left(b'-\mathcal{I}\psi^2\right)=\frac{1}{\chi^2}\left(b'-\mathcal{I}\psi^2\right)$$

With boundaries conditions:

$y=\mu$:

$$b_0+c_0\simeq b_\mu+c_\mu$$

$$\left(\frac{\partial b}{\partial y}\right)_\mu+\left(\frac{\partial c}{\partial y}\right)_\mu=-\psi$$

$$b_\mu = -\frac{1}{\sqrt{\pi}}\int_0^\tau \left(\frac{\partial b}{\partial y}\right)_\mu \frac{1}{\sqrt{\tau-\eta}}d\eta \text{ and } c_\mu = -\frac{1}{\sqrt{\pi}}\int_0^\tau \left(\frac{\partial c}{\partial y}\right)_\mu \frac{1}{\sqrt{\tau-\eta}}d\eta \text{ i.e. } b_\mu + c_\mu = \mathcal{I}\psi$$

$$Kb_\mu = c_\mu^2 \quad \text{and} \quad K\left(\frac{\partial b}{\partial y}\right)_\mu = 2c_\mu\left(\frac{\partial c}{\partial y}\right)_\mu$$

Thus:

$$b_\mu + \sqrt{Kb_\mu} = \mathcal{I}\psi \quad \text{and} \quad \left(\frac{\partial b}{\partial y}\right)_\mu = \frac{-\psi}{1+\frac{1}{2}\sqrt{\frac{K}{b_\mu}}}$$

$$b_\mu = \frac{K}{4}\left(\sqrt{1+4\frac{\mathcal{I}\psi}{K}}-1\right)^2 \simeq \frac{\mathcal{I}\psi^2}{K} \text{ because } b_\mu \to 0 \text{ and } \mathcal{I}\psi \text{ is finite.}$$

Then:

$$\left(\frac{\partial b}{\partial y}\right)_\mu = \frac{-\psi}{1+\frac{1}{2}\sqrt{\frac{K}{b_\mu}}} \simeq \frac{-2\psi}{K}\mathcal{I}\psi << \psi$$

leading to the following limit conditions:

$$y' = 0 : \psi = -\left(\frac{\partial b'}{\partial y'}\right)_0$$

$$y' \to \infty : \left(\frac{\partial b'}{\partial y'}\right) \to 0 \quad b' \to \mathcal{I}\psi^2$$

$$\xi' = \ln\left(\frac{a_0}{b'_0}\right)$$

Taking into account those conditions we obtain:

$$b'_0 = \chi\psi + \mathcal{I}\psi^2$$

and the equation of the voltammogram in the **KE zone** is:

$$1-\mathcal{I}\psi = \left(\chi\psi + \mathcal{I}\psi^2\right)\exp(\xi') \text{ with } \xi' = \xi - \ln K$$

Two limiting behaviors can be achieved:

If $\chi \to 0$ then $1-\mathcal{I}\psi = \mathcal{I}\psi^2\exp(\xi')$ the DE zone voltammogram's equation is recovered

If $\chi \to \infty$ then $1-\mathcal{I}\psi = \dfrac{\psi\exp(\xi)}{\sqrt{\lambda_+}}$ the KP zone voltammogram's equation is recovered

We have thus proved that in the transition KE zone between the DE and KP zones, the system depends on the value of a single parameter: $\chi = \frac{K}{\sqrt{\lambda_+}} = \frac{\sqrt{k_+}}{k_-}\sqrt{\frac{Fv}{RT}[\mathrm{H_2O}]}$ and therefore, the boundaries between each zone is given by lines whose equations are $\log K = \mathrm{constant} + 0.5 \log \lambda_+$. The value of the constant depends on the criteria chosen for drawing boundaries in the zone diagram (typically a ±5 mV uncertainty in the peak potential measurements).

Using Digielch simulation program,[11] the zone diagram for the EC$_{-2}$ mechanism can be drawn; and it is sketched in figure S9. In the case of the transition between KE and DE zones, the boundary equation is: $\log K = \text{-}1 + 0.5 \log \lambda_+$ i.e. a transition for a parameter: $\chi = 0.1$.

b. Use of the zone diagram to analyze experimental data:

It appears on the zone diagram that increasing the concentration of water induces a displacement in the zone diagram from the upper zone to the lower zone (increase of K) and also from the left side to the right side (increase of λ_+). The kinetics influence of the follow-up reaction requires the constant K to be larger than 0.3 which is achieved when the concentration of H_2O is large enough. In this condition, we can consider that $K > 0.3$ and $\lambda_+ = \frac{RT}{Fv} k_+ [\mathrm{H_2O}] > 1$. The observation of a thick, almost reversible, wave in presence of 10 M of water (see figure 2a in the text) thus corresponds a system close to the DE/KE boundary. Starting for example from the DE zone (cross A in red in the diagram), an increase of the concentration of water, which increases by the same value $\log K$ and $\log \lambda_+$ leads to a system that comes closer and closer to the boundary between DE and KE zones and ultimately ends up in the KE zone (cross B in red in the diagram) as observed experimentally in figure 2b from the shape of the voltamogramm. Indeed it can be seen on the diagram that as soon as $\log \lambda > 1.5$, the boundary between DE and KE zone is given by $\log K = -1 + 0.5 \log \lambda$ while the displacement upon water concentration increase corresponds to a straight line with a slope of 1.

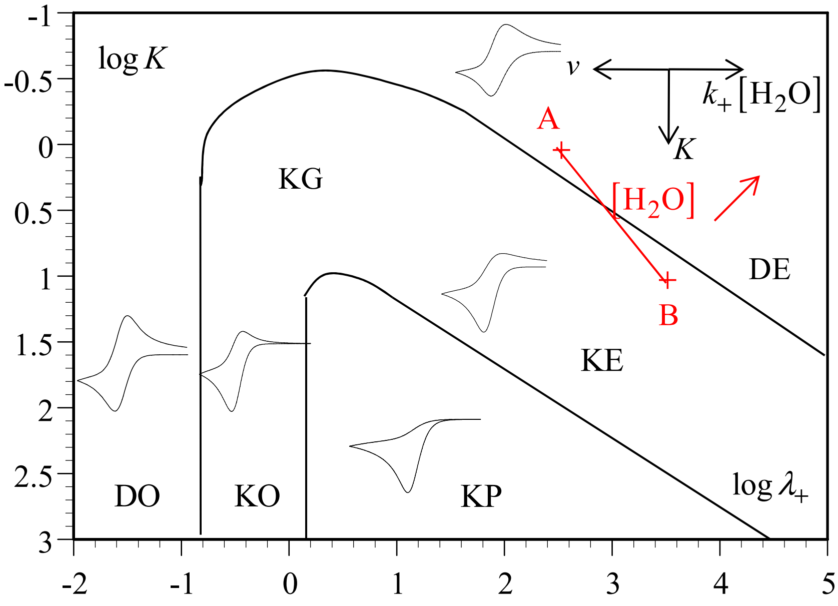

Figure S9. Zone diagram for an EC$_{-2}$ mechanism.

As discussed in section (a), in the KE zone, the system depends on a single parameter $\chi = \frac{K}{\sqrt{\lambda_+}} = \frac{\sqrt{k_+}}{k_-}\sqrt{\frac{Fv}{RT}[H_2O]}$. Simulations using Digielch program shows that the shapes of the voltammograms shown in figure 2a, recorded at $v = 0.1$ V/s and T = 293 K, are reproduced for a value of $\frac{K}{\sqrt{\lambda}} \simeq$ 0.8 for [H_2O] = 20 M and $\frac{K}{\sqrt{\lambda}} \simeq 0.56$ for [H_2O] = 10 M (figure S10) in agreement with the qualitative prediction from the zone diagram (just below the DE/KE boundary).

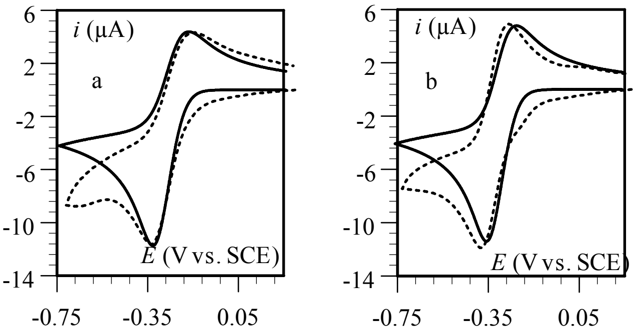

Figure S10. Cyclic voltammetry of **1** (1 mM) at 0.1 V/s, T=293 K, on a glassy carbon electrode in CH_3CN + 0.1 M NBu_4PF_6. dashed lines: experimental data; full lines : simulations. (a) **1** + 20 M H_2O, simulation with . $\frac{K}{\sqrt{\lambda}} \simeq$ 0.8 (b) **1** + 10 M H_2O; simulation with . $\frac{K}{\sqrt{\lambda}} \simeq$ 0.56. (simulations performed with a guess value $k_+ = 500$ M^{-1} s^{-1}).

We thus obtain $\frac{\sqrt{k_+}}{k_-} \simeq$ 0.09 but k_+ and k_- cannot be determined separately from those experiments.

c. Kinetic Isotope Effect:

Assuming that there is no thermodynamics isotope effect, simulations have been done with the same parameter K as above but the value of the competing parameter $\frac{K}{\sqrt{\lambda}}$ has been adjusted (i.e. by changing k_+ value) so as to reproduce the shapes of the voltammogramms, i.e. the anodic peaks, as shown on figures S11 and S12. We obtain:

$KIE(H/D) = \frac{k_{+,H}}{k_{+,D}}$ around 2 and $KIE\left({}^{16}O/{}^{18}O\right) = \frac{k_{+,{}^{16}O}}{k_{+,{}^{18}O}}$ larger than 5.

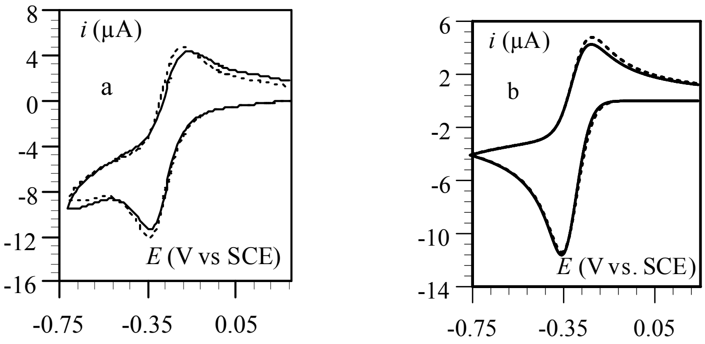

Figure S11. Cyclic voltammetry of **1** at 0.1 V/s, *T*=293 K, on a glassy carbon electrode in CH_3CN + 0.1 M NBu_4PF_6. Dashed line: in presence of 10 M of H_2O ; solid line: in presence of 10 M of D_2O. (a) experiments (b) simulations.

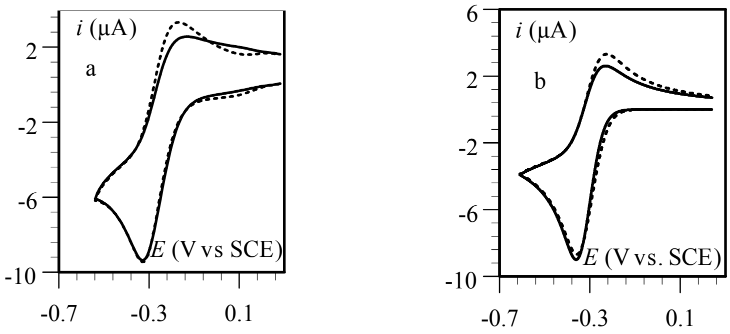

Figure S12. Cyclic voltammetry of **1** at 0.1 V/s, *T*=293 K, on a glassy carbon electrode in CH_3CN + 0.1 M NBu_4PF_6. Dashed line: in presence of 10 M of $^{16}OH_2$; solid line: in presence of 10 M of $^{18}OH_2$. (a) experiments (b) simulations.

VIII. Variation of the Mn(III)/Mn(II) wave upon of addition of $HClO_4$.

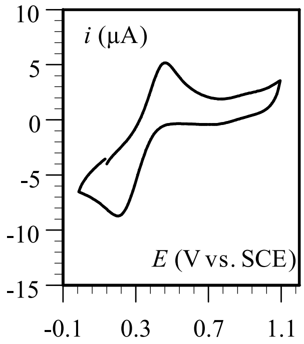

Figure S13. Cyclic voltammetry of 1 mM of $\mathbf{1}^+$ (wave 1/1') at 0.1 V/s, T=293 K, on a glassy carbon electrode in CH_3CN + 0.1 M NBu_4PF_6 after addition of 1 mM $HClO_4$. Upon acidification, a new wave appears (wave 2/2'), corresponding to the formation of $[Mn(III)(OH_2)]^{2+}$, with $E^0_{Mn^{III}OH_2/Mn^{II}OH_2}$ = + 0.32 V vs. SCE.

IX. Comment on reaction 3-1:

$$\begin{tikzcd}
{[Mn^{III}OH]^+ + H_2O^*} \arrow[rr, shift left] \arrow[dr, shift left, "(3\text{-}2)"'] & & {[Mn^{III}O^*H]^+ + H_2O} \arrow[ll, shift left] \arrow[dl, shift left] & (3\text{-}1) \\
& {[Mn^{III}O^*H_2]^{2+} + HO^-} \arrow[ul, shift left] \arrow[ur, shift left, "(3\text{-}3)"'] & &
\end{tikzcd}$$

Reaction (3-1) is an isotope exchange reaction, therefore $K_{3-1} = 1$.

In presence of a strong acid we have shown that: $E^0_{Mn^{III}OH_2/Mn^{II}OH_2} = 0.32$ V vs. SCE (see figure S13)

In presence of water (10 M), we can see on figure 2a that: $E^0_{Mn^{III}OH+H_2O/Mn^{II}OH_2+OH^-} = -0.35$ V vs. SCE.

$$\begin{tikzcd}
{[Mn^{III}OH]^+ + H_2O + e} \arrow[rr, shift left] \arrow[dr, shift left, "(3\text{-}2)"'] & & {[Mn^{II}OH]^+ + HO^-} \arrow[ll, shift left] \arrow[dl, shift left] \\
& {[Mn^{III}OH_2]^{2+} + HO^- + e} \arrow[ul, shift left] \arrow[ur, shift left] &
\end{tikzcd}$$

Thus, from the above thermodynamics cycle we have:

$$\log K_{3-2} = \log\left(\frac{1}{K_{3-3}}\right) = \frac{F}{RT\ln 10}\left(E^0_{Mn^{III}OH+H_2O/Mn^{II}OH_2+OH^-} - E^0_{Mn^{III}OH_2/Mn^{II}OH_2}\right) = -11.15$$

References

1. J. F. Larrow, E. N. Jacobsen, Y. Gao, Y. Hong, X. Nie and C. M. Zepp, *J.Org.Chem.*, 1994, **59**, 1939-1942.
2. O. Horner, E. Anxolabéhère-Mallart, M.-F. Charlot, L. Tchertanov, J. Guilhem, T. A. Mattioli, A. Boussac and J.-J. Girerd, *Inorg. Chem.*, 1999, **38**, 1222-1232.
3. G. M. Sheldrick, University of Göttingen, Göttingen, Germany, 1997.
4. L. J. Farrugia, *J. Appl. Cryst.*, 1997, **30**, 565.
5. C. Hureau, L. Sabater, E. Anxolabéhère-Mallart, M. Nierlich, M.-F. Charlot, F. Gonnet, E. Rivière and G. Blondin, *Chem.-Eur. J.*, 2004, **10**, 1998-2010.
6. C. Hureau, S. Blanchard, M. Nierlich, G. Blain, E. Rivière, J.-J. Girerd, E. Anxolabéhère-Mallart and G. Blondin, *Inorg. Chem.*, 2004, **43**, 4415-4426.
7. C. Hureau, G. Blondin, M.-F. Charlot, C. Philouze, M. Nierlich, M. Césario and E. Anxolabéhère-Mallart, *Inorg. Chem.*, 2005, **44**, 3669-3683.
8. L. Sabater, C. Hureau, G. Blain, R. Guillot, P. Thuéry, E. Rivière and A. Aukauloo, *Eur. J. Inorg. Chem.*, 2006, 4324-4337.
9. J.-M. Savéant, in *Elements of Molecular and Biomolecular Electrochemistry*, ed. Wiley-Interscience, New York, 2006.
10. C. Amatore, D. Garreau, M. Hammi, J. Pinson and J.-M. Savéant, *J. Electroanal. Chem.*, 1985, **184**, 1-24.
11. M. Rudolph, *J. Electroanal. Chem.*, 2003, **543**, 23.